Characterization of accessible and inaccessible pores in microporous carbons by a combination of adsorption and small angle neutron scattering

Thanh X. Nguyen, Suresh K. Bhatia *

School of Chemical Engineering, The University of Queensland, Brisbane, QLD 4072, Australia

ARTICLE INFO

ABSTRACT

We determine the pore size distribution for five activated carbons (comprising carbide derived as well as commercial activated carbon samples) by the interpretation of experimental small angle neutron scattering (SANS) intensity profiles, based on the primary assumption of an infinitely dilute solution of hollow spherical particles. The interpretation yields the pore size distribution of the carbon samples that have predominantly micropore populations (size <20 Å), but not for carbons which have significant mesopore populations of sizes up to 48 Å and high mass fractal degrees. The pore size distribution (PSD) results based on SANS data reveal significant populations of micropores of size <6.1 Å, and mesopores of size >20 Å, which are not present in the PSD results based on adsorption isotherms of either Ar at 87 K or CO_2 273 K. This inaccessible porosity becomes accessible to CO_2 and Ar on heat treatment, leading to increase in the adsorption based pore volume. However, the surface area does not commensurately increase, indicating the inaccessible microporosity to predominantly comprise surface defects and roughness that are removed on heat treatment or activation. This finding sheds the light onto the evolution of porosity of activated carbons during gasification or post synthesis-treatment.

1. Introduction

Microporous carbon has superior absorptive abilities that make it one of the most versatile materials in processes for fluid separation, molecular sieving, gas storage and catalysis [1]. However, it has an inherently complex, disordered structure, with localized buckling and other distortions [2,3]. Such distortions lead to defects and constrictions that restrict the most commonly used probing gases (Ar and N_2) for accessing the entire carbon microstructure within experimental time scales at subcritical conditions [4–6]. This gas accessibility problem leads to difficulty in the accurate characterization of porous carbons including coals and molecular sieve carbons (MSC) by the gas adsorption technique, especially of the pore throats in these carbons. The narrow pore entries,

whose free diameter is very similar to the molecular dimension of simple gases such as Ar, N_2, CO_2, and CH_4, have theoretically been shown [7] to dictate the separation factor for gas mixtures. Thus, the accurate characterization of the molecularly restrictive pore throats in activated carbons is vital to capture true adsorption dynamics in the MSCs or coals.

Small angle X-ray (SAXS) and neutron scattering (SANS) techniques, free from the above accessibility issues, offer attractive alternatives for achieving the rigorous characterization for the microstructure of porous carbons. Such small angle scattering (SAS) methods have been widely utilized to complement adsorption techniques for this task [8–12]. Among these, SANS has an advantage over the SAXS in determining the dimension of molecularly narrow pore

spaces, because neutrons do not carry charge and can therefore penetrate deeply inside the atom and directly interact with its nucleus without the interference of electron clouds. Owing to the very short range of the neutron–nucleus interaction, interatomic distance is accurately probed by the neutron scattering technique and, therefore, so is the carbon center-to-center diameter of pore spaces. On the contrary, since an electron carries negative charge it interacts only with the outer electron cloud, and not with the nucleus of the atom. Consequently, it is the free diameter of pore spaces, or the accessible pore width, that is probed by the X-ray scattering technique. However, the outer electron cloud of an atom can be significantly distorted as it forms chemical bonds with other atoms. This leads to difficulty in accurately determining the width of molecularly constricted pore spaces formed by the disordered arrangement of a few carbon atoms.

While, in principle, small angle scattering (SAS) methods, especially SANS, have an advantage over the adsorption technique as discussed above, in practice the interpretation of SAS data for the pore size distribution is much more complex and very challenging. This is due to both the highly disordered nature and the extremely high micro-porosity of porous carbons. As a result, SAS data have normally been utilized to estimate the overall macroscopic properties of porous carbons such as effective dimension particle size, porosity, specific surface area, mass or surface fractal [8,10,12]. More recently, there have been a few studies which have attempted to determine the pore size and pore wall distributions of activated carbons by the interpretation of SAXS [11] and SANS data [12]. Among these, Gun'ko et al. [11] solved for the pore size distribution of polymer derived activated carbons and their polymeric precursor (porous phenol formaldehyde resin beads, termed carbonizate) by matching the theoretical and experimental total scattering intensities over the Porod region corresponding to the wave vector magnitude $q < 1.25$ Å^{-1}. The theoretical intensity was calculated based on the assumption of an infinitely dilute solution of polydisperse hollow spheres. These authors achieved reasonable similarity between the shape of the PSD results obtained from SAXS and that from the nitrogen adsorption at 77 K only for the large micropore region (width >10 Å). However, for the ultra-micropore region (width <10 Å), the PSD results obtained from SAXS for the carbonizate and its derivatives were very different from those based on the nitrogen adsorption technique. In particular, the former has only a single peak located at a pore size of 5 Å or pore width of 1.4 Å in this ultramicropore region while the latter has significant pore populations in this region. However, no explanation for these inconsistent results was offered by the authors.

This study focuses on determining the pore size distribution for microporous carbons based on the interpretation of SANS data. Five microporous carbon samples comprising of a SiC-CDC-800, a heat-treated Ti$_3$SiC$_2$-CDC-800-H1, three activated carbons (ACF-15, Takeda 3 Å, and BPL) have been investigated. In our recent works [13–17], the PSD results of SiC-CDC-800, Takeda 3 Å, and ACF-15, determined by the adsorption technique of Ar at 87 K or CO$_2$ at 273 K, have shown the predominance of micropores, while those of Ti$_3$SiC$_2$-CDC-800-H1 and BPL carbons display significant mesopore populations sized up to 48 Å. With the choice of the carbon samples

examined in the current work, the comparison between the PSD results obtained from SANS and those from the adsorption technique helps elucidate the above issue of differences between the two methods in the ultra-micropore region. Furthermore, except for the ACF-15 carbon, the other examined samples are partially inaccessible to methane. Thus, the PSD analysis for these examined carbons using SANS measurements free from the gas accessibility problem is critical for the understanding of gas adsorption behavior in these carbons, as well as for facilitating the optimal design of nanoporous carbons for gas and liquid mixture separations.

2. Experimental

2.1. Materials

Five activated carbon samples were subjected to small angle neutron scattering (SANS) measurements. These comprised one SiC-CDC-800, one heat-treated carbon sample (Ti$_3$SiC$_2$-CDC-800H1), and three commercial activated carbons: molecular sieve carbon (MSC) Takeda 3 Å, BPL carbon, and activated carbon fiber ACF-15. The first two carbon samples were recently prepared in our laboratory [14–15]. In brief, the SiC-CDC-800 and Ti$_3$SiC$_2$-CDC-800H1 samples were synthesized from commercial 5 nm sized βSiC [14] and 6μ Ti$_3$SiC$_2$ (3-ONE-2, LLC, Voorhees, NJ) [15] powders, provided by Sigma–Aldrich, respectively. Chlorination experiments were performed on these carbide powders using high purity chlorine (BOC Gases, 99.5%) and high purity argon (BOC Gases, 99.998%) as reactive and purging gases, respectively. 12 g of the carbide powders was placed onto a quartz sample boat and loaded into the hot zone of a horizontal quartz tube furnace. The tube was initially purged by argon for 30 min before heating rate of 30 °C per minute was employed to raise temperature of the furnace to the desired chlorination one. The chlorination experiment began once the desired temperature (800 °C) was reached and stabilized as well as argon flow was stopped. In the chlorination experiment, pure Cl$_2$ gas was flowed thorough the carbide sample at the rate of 50 ml per minute until the chlorination reaction of the carbide sample was completed. After the completion of the chlorination reaction, the Ar flow was used to cool the sample down to ambient temperature as well as flush metal chlorides remaining in the sample. The residual chlorine and metal chlorides were captured in sodium chloride solution. The carbon sample (Ti$_3$SiC$_2$-CDC-800 H1) was prepared by the heat treatment of the virgin Ti$_3$SiC$_2$-CDC-800 carbon sample at 1100 °C for 1 day in argon atmosphere with constant flow of pure argon at 50 ml/min [15].

2.2. Characterization

Of the carbon samples subjected to the small angle neutron scattering measurements, the activated carbon fiber ACF-15 is in fibrous form while the other carbon samples are in powder form. The ACF-15 sample is originally in the form of carbon cloth. The fibers of the ACF-15 were separated from the carbon cloth and subsequently cut into 1 mm long fibers. The average particle size of BPL and MSC Takeda 3 Å is about

50 μm. The SiC-CDC-800 and Ti_3SiC_2-CDC-800 H1 samples are in very fine powder forms. The carbon samples examined in this work were degassed at 300 °C overnight and subsequently subjected to small angle neutron scattering measurements using the D16 instrument at the Institut Laue Langevin (ILL), Grenoble. The degassed samples were contained in low boron glass NMR tubes of 5 mm external diameter and sealed by paraffin paper. The scattering intensities of each carbon sample was measured in two separate wave vector q ranges ($0.02\,\text{Å}^{-1} < q < 1.2\,\text{Å}^{-1}$) and ($0.1\,\text{Å}^{-1} < q < 2.5\,\text{Å}^{-1}$), where $q = (4\pi/\lambda)\sin(\theta/2)$, θ is the scattering angle and λ ($=4.75\,\text{Å}$) is the wave length of the incident neutron beam. The scattering intensity recorded on each detector cell was corrected for electronic and ambient background by means of measurements using a cadmium plate (approximately 2×6 cm) and the scattering contribution of an empty cell. The scattering intensity of water was also measured to acquire the normalized scattering intensities on each detector cell in absolute units (cm^{-1}). These normalized scattering intensities were then radially averaged around the beam centre of the detector to obtain a one-dimensional data, q-dependent total scattering intensity. The two total scattering intensities measured in the two separate wave vector q ranges, as mentioned above, were merged to obtain the total scattering intensity in the wave vector region ($0.02\,\text{Å}^{-1} < q < 2.5\,\text{Å}^{-1}$). Finally a flat incoherent background was subtracted from the total scattering intensity of each carbon sample. The estimation of this flat incoherent background is given in Section S1 and Fig. S1 of the Supporting Information.

3. Results and discussion

3.1. Average characteristic properties

In this sub-section, we interpret the SANS data for the effective size of carbon particles and pore shapes in the examined carbon samples. These SANS data have been plotted on logarithmic axes, as shown in Fig. 1. It can be seen that there are two different wave vector regions: Region I ($0.02\,\text{Å}^{-1} < q < 0.05\,\text{Å}^{-1}$) and Region II ($0.1\,\text{Å}^{-1} < q < 1.0\,\text{Å}^{-1}$) [18]. We fitted the total scattering intensity of all the carbon samples to a power law ($I(q) \sim q^{-n}$) in these regions. The fits are depicted by solid lines in Fig. 1. The total scattering intensity in Region I mainly arises from correlations between carbon particles. All the values of the power law exponent, n, derived from the fits in Region I are given in Table 1. It can be seen that the scattering intensity of the SiC-CDC-800 and the MSC Takeda 3 Å conform to the power law with exponent values n approaching 4, indicative of a smooth surface of carbon particles in these samples. The latter is consistent with the graphitized surface of particles in the SiC derived carbon, as reported in our recent work [14] and elsewhere [19]. The MSC Takeda 3 Å contains a majority of ultra-micropores (pore width <8 Å) which may reduce the mass or surface fractal degrees. On the contrary, the scattering intensity of the BPL and Ti_3SiC_2-CDC-800H1 samples conforms to the power law with exponent n having values around 2.5, indicating high mass fractal degree of these two samples. This is also consistent
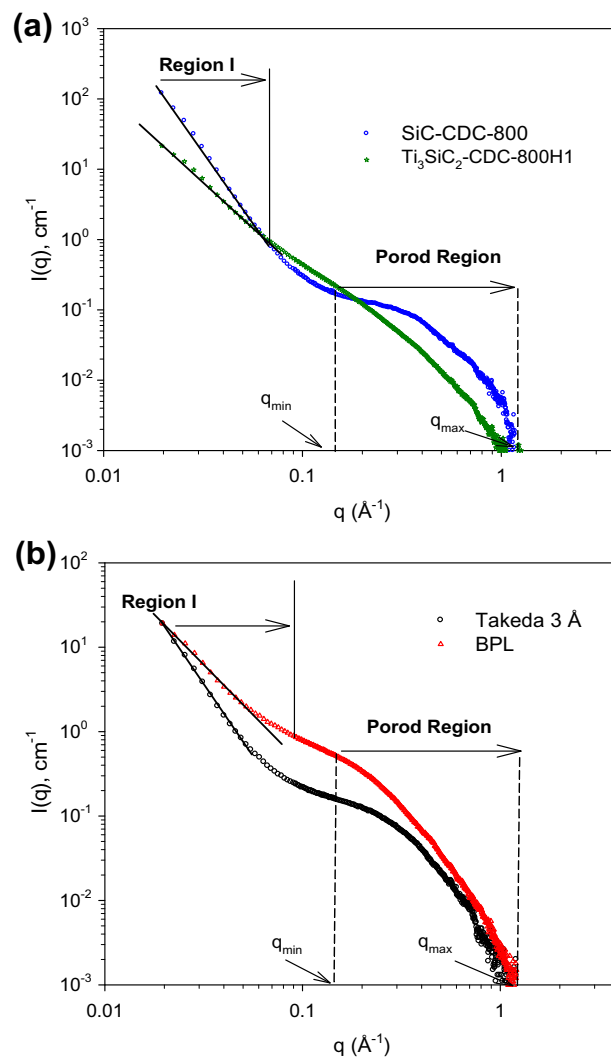
Fig. 1 – Total neutron scattering intensities of all the examined carbon samples against the magnitude of wave vector, q, plotted on logarithmic axes.

with significant mesopore populations found in the pore size distribution results of these samples, obtained from Ar adsorption technique at 87 K reported in our previous works [15,16].

Furthermore, the total scattering intensities of the examined carbon samples were fitted to a Guinier equation over the q-range 0.02–0.035 Å^{-1}, following

$$I(q) = I_0 \exp\left[-\frac{(qR_G)^2}{3}\right] \quad (1)$$

to obtain the radius of gyration of the carbon particles, R_G, where I and I_0 are the intensity of scattered and incident neutron beams. Fig. S2(a) and (b) in Supplementary content show the fits of the experimental scattering intensities of the four carbon samples (SiC-CDC-800, Ti_3SiC_2-CDC-800H1, MSC Takeda 3 Å, and BPL) to the Guinier equation. Accordingly, the effective size (d_c) of carbon particles in these samples was estimated through the following relation with the assumption of spherical shape of carbon particles [18]

Table 1 – The values of the exponent n derived from fits of the experimental neutron scattering intensities to the power law equation ($I(q) \sim q^{-n}$).

Sample name	Guinier region		Porod region	
	$0.01\,\text{Å}^{-1} < q < 0.1\,\text{Å}^{-1}$	$0.1\,\text{Å}^{-1} < q < 0.35\,\text{Å}^{-1}$	$0.35\,\text{Å}^{-1} < q < 0.65\,\text{Å}^{-1}$	$0.7\,\text{Å}^{-1} < q < 1.0\,\text{Å}^{-1}$
SiC-CDC-800	3.97	1.08	2.50	4.00
Ti$_3$SiC$_2$-CDC-800H1	2.56	2.10	3.00	4.00
Takeda 3 Å	3.44	1.60	3.00	4.20
BPL	2.44	2.05	3.00	4.20
ACF-15	No data	1.10	3.00	4.20

$$d_c = 2R_G \sqrt{5/3} \tag{2}$$

The estimated effective sizes of carbon particles in the SiC-derived carbon and Takeda 3 Å samples in the range, 141–153 Å, are significantly larger than for BPL and Ti$_3$SiC$_2$-CDC-800H1 samples (112 Å–118 Å). While scattering data in the small q region ($q < 0.02\,\text{Å}^{-1}$) may help in reliable estimation of these effective sizes of the carbon particles (118–153 Å), as mentioned above, its absence in the present case may have insignificant impact on the accuracy of the results of these effective particle sizes. The latter is due to the strong linear correlation of the available scattering data in the q range of 0.02–0.035 Å^{-1}. This is consistent with the high mass fractal degrees of the latter samples, as indicated above.

The intensity in the Region II or Porod region ($0.1\,\text{Å}^{-1} < q < 1.0\,\text{Å}^{-1}$) is mainly the consequence of scattered neutrons from the internal surface of micro- and meso-pores. The values of the power exponent n determined from the fits of the coherent scattering intensity of the examined carbon samples to the power law form in this region are presented in Table 1. From Fig. S3 in the Supplementary content, it can be clearly seen that there are three subregions, corresponding to ultramicropores (size <8.5 Å, or $0.75\,\text{Å}^{-1} < q < 1.0\,\text{Å}^{-1}$), micropores (10 Å < size < 18 Å, or $0.35\,\text{Å}^{-1} < q < 0.65\,\text{Å}^{-1}$), and mesopores (size >20 Å or $0.1\,\text{Å}^{-1} < q < 0.35\,\text{Å}^{-1}$). These fits are illustrated by dashed lines in Fig. 1 and Fig. S3. From Table 1, the power law exponent, n, of all the examined carbon samples ranges from 1 to 2 for the mesopore region, but from 2.5 up to the expected value (4) for micro- and ultramicro-pore regions, indicating high mass fractal degrees of carbon particles in these samples at microporous scales. More interestingly, in the mesopore range the exponent, n, of the carbon samples (SiC-CDC-800 and ACF-15 Å) approaches unity while that of the carbon samples (Ti$_3$SiC$_2$-CDC-800H1 and) is around 2, as shown in Table 1. The former reveals the cylinder-like shape of pore spaces in these samples while the latter indicates slit-like pore geometry. This may be due to the higher degree of graphitisation of the Ti$_3$SiC$_2$-CDC-800H1 and BPL at the mesopore scale ($q < 0.35\,\text{Å}^{-1}$ or the pore size >18 Å) compared to that of the remaining carbon samples (SiC-CDC-800 and Takeda 3 Å carbons). The higher degree of graphitisation of the Ti$_3$SiC$_2$-CDC-800H1 and BPL samples can be evidenced through sharper 002 reflections of the XRD patterns of these samples compared to that of the SiC-CDC-800 sample, as shown in Fig. S4. Furthermore, the helium densities of these carbons (Ti$_3$SiC$_2$-CDC-800H1 and BPL) of 2.35 g/cm^3 and 2.12 g/cm^3 respectively, as shown Table S1, are very close to that of graphite (2.27 g/cm^3). On the other hand, the lower values of the exponent n of the remaining carbon samples may be due to the disordered nature of these carbons at the mesoporous scale, which most likely comprise curved and/or twisted carbon walls, leading to their cylinder-like geometry. Despite the higher degree of graphitization at the mesopore scale of the carbon samples (Ti$_3$SiC$_2$-CDC-800H1 and BPL) compared to the remaining carbon samples, these two former carbons have an overall disordered character. This is due to the fact that the exponent, n, at micropore scale ($q > 0.35\,\text{Å}$ or pore size >18 Å), as shown in Table 1, varies from 3 to 4, indicating the disordered nature of the Ti$_3$SiC$_2$-CDC-800H1 and BPL samples at this scale. Accordingly, the predominant population of micropores in these carbons, as seen in their PSD results obtained by the adsorption technique of Ar at 87 K [14–15] or CO$_2$ at 273 K [17], is clearly indicative of their disordered nature.

3.2. Pore size distribution

In this sub-section, we determine the pore size distribution of all the examined samples based on the small angle neutron scattering measurements, as shown in Fig. 1, by minimizing the deviation, δ, between theoretical (I_{theor}) and experimental (I_{exp}) coherent scattering intensities over the Porod law region ($q_{min} < q < q_{max}$)

$$\delta = ||I_{theor}(q) - I_{exp}(q)|| \tag{3}$$

coupled with Tikhonov regularization. The L-curve technique [20] is used for determining the regularization parameter. As discussed in the above Section 3.1, carbon particles of the examined samples showed high degrees of surface fractals at microporous scales. Furthermore, micropore populations in these carbons are predominant. Accordingly, the theoretical coherent scattering intensity was calculated by considering the carbon microstructure as an infinitely dilute solution of polydisperse hollow spherical particles [18] with distribution $\gamma(R)$, and whose radius ranges from R_{min} ($=\pi/q_{min}$) to R_{max} ($=\pi/q_{max}$)

$$I_{theor}(q) = C\varnothing\Delta\rho^2 \int_{R_{min}}^{R_{max}} dR\gamma(R)\left(\frac{4\pi}{3}\right)R^3 P(qr)S(q) \tag{4}$$

where the structure factor $S(q)$ approaches unity at large q ($\rightarrow\infty$) such that the inter-distance between pore spaces is large compared to their sizes. From Eq. (4), it can be seen that the pore volume $v = \int_{R_{min}}^{R_{max}} dR\gamma(R)\left(\frac{4\pi}{3}\right)R^3$. Accordingly, the pore size distribution, $f(D)$, can be given as

$$f(D) = dv/dD = 2\gamma\left(\frac{D}{2}\right)\left(\frac{\pi}{6}\right)D^3 \qquad (5)$$

Thus, Eq. (4) can be rewritten by the use of Eq. (5)

$$I_{theor}(q) = C\varnothing\Delta\rho^2 \int_{D_{min}}^{D_{max}} dD f(D)P(qD/2) \qquad (6)$$

where $\varnothing$ is porosity, and $\Delta\rho^2$ is the contrast factor, defined as

$$\Delta\rho^2 = (b_c\rho_c)^2 \qquad (7)$$

where b_c and ρ_c are the scattering length and density of the carbon solid phase, respectively. The latter is assigned as the helium density, assuming complete accessibility to He. C is a normalization factor, which depends on the apparent density of samples in the sample tube and the scattering volume with neutron beam, and is unknown. The focus of this work is to compare the shape of the pore size distribution results determined from the experimental SANS data with those obtained from the experimental adsorption isotherms. Accordingly, the normalization factor, C, in Eq. (6) is used as a fitting parameter such that the specific pore volume determined by SANS is close to that obtained by the adsorption technique over the microporous range (size <20 Å) accessible by the probing gas. It is noted that the size of a graphitic slit-pore, D, is defined as the carbon centre–carbon centre distance separating its two opposing carbon walls. The pore width of the graphitic slit-pore, H_{in}, is approximately determined by subtracting the LJ collision diameter of carbon atom in the graphite, $\sigma_{C-C} = 3.4$ Å, from the center–center pore size. The choice of specific pore volume for this fitting task is due to the fact that it is not sensitive to the choice of pore wall thickness in the DFT interpretation of adsorption isotherms.

The form factor $P(qR)$ is given [18] as

$$P(qR) = 9\frac{(\sin(qR) - qR\cos(qR))^2}{(qR)^6} \qquad (8)$$

All the carbon samples examined contain principally micro and meso-pores whose size is less than 50 Å, as determined in our recent works using the adsorption technique. Accordingly, q_{min} is assigned a wave vector value within the q-range of 0.13-0.14 Å^{-1} while q_{max} is taken as 1.25 Å^{-1} to minimize the influence of the wide angle scattering signal [11]. The choice of q_{min} should be made to minimize the amount of mesopores formed between carbon grains or inter-particle mesopores. A large amount of inter-particle mesopores may lead to the invalidity of the assumption of an infinitely dilute solution of polydisperse hollow spherical particles made in Eq. (6). This choice of q_{min} enables one to probe a maximum pore diameter ($D_{max} = 2\pi/q_{min}$) in the pore size range of 45–48 Å which generally suffices to cover the pore size range of microporous carbons. The choice of q_{max} (=1.25 Å) allows detection of the smallest pore size down to 5 Å^{-1}. For convenience, the pore size distribution result determined from the SANS data is named as SANSPSD, while that obtained from the adsorption isotherm of Ar at 87 K or CO_2 at 273 K using the slit-pore model is named as Ar87PSD or $CO_2$273PSD, respectively.

The Ar87PSD and $CO_2$273PSD results of the examined carbon samples (SiCDC-800, Ti$_3$SiC$_2$-DC-800H1, BPL, MSC Takeda 3 Å, and ACF-15) were taken from our previous works [14,16–17]. In particular, these Ar87PSD results were obtained

for the four carbon samples (SiCDC-800, Ti$_3$SiC$_2$-DC-800H1, BPL, and ACF-15) by the interpretation of the adsorption isotherms of Ar at 87 K using the Finite Wall Thickness (FWT) model [16]. These Ar adsorption isotherms were measured using a Micromeritics Adsorption Analyser ASAP 2020, and are given in Fig. S5(a) of the Supporting Information section. Furthermore, the $CO_2$273PSD result of the MSC Takeda 3 Å sample was determined [17] by the interpretation of the high pressure adsorption isotherm of CO_2 at 273 K, as depicted in Fig. S5(b), using the Infinite Wall Thickness model.

3.2.1.　SiC-CDC-800

Fig. 2 depicts the comparison between the SANSPSD and Ar87PSD results of the SiC-CDC-800 sample. The AR87PSD result of this sample was reported in our recent work [14]. From this figure, it is interesting to see excellent agreement between the SANSPSD and Ar87PSD results over the accessible pore size regions (3.4 Å < width < 20 Å). Significantly higher intensity of the first peak in the Ar87PSD result of this carbon compared to that in the SANSPSD result is due to weaker carbon-Ar interaction strength used by the slit-pore model [13]. The actual carbon surface is normally curved due to defectives (irregular rings or missing carbon atoms), enhancing its interaction strength with Ar compared to that of the smooth graphitic surface [13]. The use of the weak carbon-Ar interaction strength by the slit-pore model to fit the experimental Ar adsorption data artificially increases the population of smallest pores, represented by the first peak in the Ar87PSD result, in which the carbon-Ar interaction strength is strongest. The SANSPSD result further reveals significant porosities in the small pore region (width <3.4 Å) inaccessible to Ar at 87 K, and in the mesopore region (width >20 Å). The mesopore population is significant in the Ar87KPSD result of these carbon samples, indicating inaccessibility of Ar at 87 K to this mesopore region. In this regard, it is likely that the small pore region inaccessible to Ar at 87 K represents the passive pore entries into this mesopore region. Thus, the
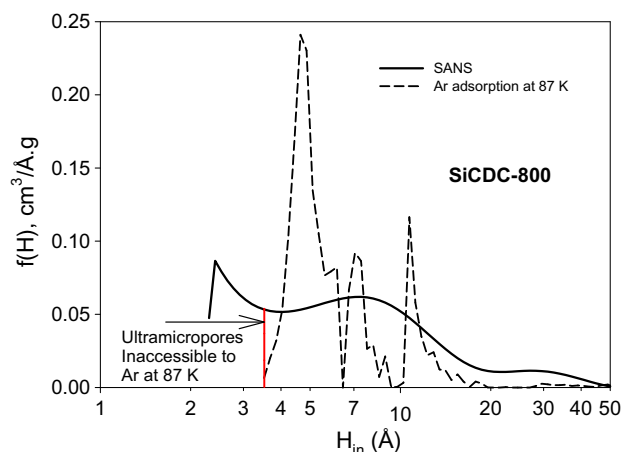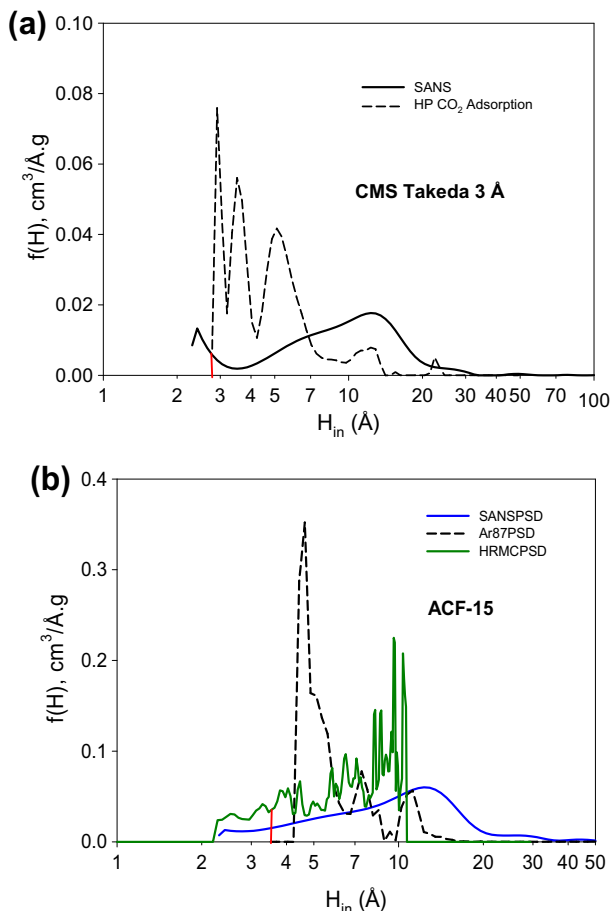

Fig. 2 – Comparison between the SANSPSD and Ar87PSD results of the SiC-CDC-800 sample. The vertical red line indicates the lowest pore width accessible to argon at 87 K. (For interpretation of the references to colour in this figure legend, the reader is referred to the web version of this article.)

deformation of this carbon under high pressure adsorption condition, as evidenced from the nonzero value of the maximum change in adsorbent volume due to deformation (ΔV_{max}) estimated for these carbon samples [14], can stem from the weak mechanical strength of these inaccessible regions compared to pore regions accessible to the adsorption. Furthermore, the small inaccessible region can be opened up during the early stage of gasification [21], leading to a significant increase in the surface area of gasified carbons compared to that of their virgin forms. On the other hand, the inaccessible mesopore region can also be opened during heat treatment [22], due to the slight enlargement of the width of their pore entries through which Ar can freely diffuse at 87 K within practical time scales.

3.2.2. Takeda 3 Å, ACF-15, and BPL

3.2.2.1. *Takeda 3 Å.* Fig. 3a shows good agreement between the SANSPSD and $CO_2$273PSD results of the molecular sieve carbon (MSC) Takeda 3 Å, only in the large pore region (width <7 Å). Surprisingly, the intensity of the population of small

Fig. 3 – (a) Comparison between the SANSPSD and $CO_2$273PSD results for CMS Takeda 3 Å, and (b) comparison between SANSPSD, Ar87PSD, and HRMCPSD results for activated carbon fiber ACF15. The vertical red lines indicate the lowest pore width accessible to (a) CO_2 at 273 K and (b) Ar at 87 K. (For interpretation of the references to colour in this figure legend, the reader is referred to the web version of this article.)

pores (2.73 Å < width < 7 Å) is significantly small compared to that of the $CO_2$273PSD result. Such significant deviation in the intensity of the small pores between the SANSPSD and $CO_2$273PSD results may be due to the rather significant amounts of noncarbon atoms in the Takeda 3 Å sample including H, O, N, and S (H/C = 0.157, O/C = 0.005, N/C = 0.01, S/C = 0.00035 in the atomic ratio, as given in Table S1). It may also be due to the presence of ash in this sample (0.61% in the weight percentage, as given in Table S1), which could contain trace amounts of metals such as V and Ni. Although lacking q-dependence, the scattering by the noncarbon atoms depends on the degree of the atomic disorder [23]. It is defined as the diffuse coherent scattering, which is q-independent and distinguishable from the true incoherent scattering arising from the isotopic and nuclear spin distributions [23]. Hence, this diffuse coherent scattering artificially enhances the true incoherent scattering intensity by carbon atoms. The total scattering intensity in the high q region (i.e. >0.6 Å^{-1}) corresponding to the small pore region (width <7 Å) predominantly comprises incoherent scattering. Accordingly, the slightly reduced accuracy in estimating the incoherent scattering intensity leads to more severe impact on the coherent intensity in this high q region. Such impact can be explained by the abnormally lower population of the small pores (2.73 Å < width < 7 Å) determined by SANS compared to that probed by Ar at 87 K. The small molecular dimension of carbon dioxide (~3.03 Å) used as a probing gas enables one to detect the smallest open pore width down to 2.74 Å or a carbon centre-to-centre pore size of 6.1 Å calculated by adding the Lennard Jones (LJ) collision diameter for carbon, $\sigma_c = 3.4$ Å, to the open pore width. However, the SANSPSD result showed a population of narrow pores (width <2.74 Å) inaccessible to CO_2 at 273 K. Indeed, our recent work [24] showed the existence of pores having centre-to-centre pore width of 5.66 Å and smaller (or open pore width of 2.26 Å and smaller), based on quantum effect mediated faster diffusion rate of deuterium (D_2) compared to of hydrogen (H_2) at 30 K, which was experimentally observed in this MSC Takeda 3 Å. This indicates that the SANS technique is very capable of detecting the pore populations inaccessible to the most commonly used probing gases such as Ar and N_2 at subcritical conditions or CO_2 at 273 K. Thus, SANS is very suitable for the characterization of porous carbons, especially molecular sieve carbons and coals.

3.2.2.2. *ACF-15.* Fig. 3b depicts the comparison between the SANSPSD and Ar87PSD results of the activated carbon fiber ACF-15 used in our recent work [25]. The pore size distribution result of the atomistic model of this carbon obtained by hybrid reverse Monte Carlo simulation [13] is named as HRMCPSD, and is shown in Fig. 3b for comparison. From this figure, much better agreement can be generally seen between the SANSPSD and the HRMCPSD than between SANSPSD and Ar87PSD. In particular, both SANSPSD and HRMCPSD results show the population of ultra-micropores (width <3.4 Å) which is completely absent in the Ar87PSD result. However, the SANSPSD result contains a small population of large pores (width >17 Å) which is not found in both the Ar87KPSD and HRMCPSD results. This is indicative of inaccessibility of Ar at 87 K to the large pore region for the case of the Ar87PSD

result. For the HRMCPSD, the high lower bound of the wave vector ($q_{min} < 0.2$ Å^{-1}) and small size of the simulation box (~30 Å) prevents the probing of this inaccessible large pore region. Despite good agreement obtained between the SANSPSD and HRMCPSD results, the intensity of the small pore population ($H_{in} < 7$ Å) in the SANSPSD result is generally lower than that in the HRMCPSD result. This is due to the impact of the scattering by noncarbon atoms (O, H, N), as discussed above, present in the activated carbon fiber ACF-15 with the atomic ratios (H/C = 0.145, O/C=, N/C = 0.004). Smaller atomic ratios of noncarbon atom to carbon atom in the ACF-15 compared to those in the Takeda 3 Å, and the absence of ash in the ACF-15 sample, suggest lesser impact of the scattering by noncarbon atoms on the true coherent intensity of carbon atoms for the ACF-15 sample than for Takeda 3 Å. This can be seen from the better agreement between the SANSPSD and Ar87PSD results in the intensity of the small pore population obtained for the ACF-15 sample compared to the Takeda 3 Å. Despite the impact of the scattering by the noncarbon atoms, a small population of the inaccessible ultra-micropores (width <3.4 Å) in the SANSPSD result is still obtained for the Takeda 3 Å carbon.

3.2.2.3. BPL.
Fig. 4 shows the comparison between the SANSPSD and Ar87PSD results of the BPL sample. From this figure, similar to the Takeda 3 Å and ACF-15 samples, the SANSPSD result shows significantly lower population of the small pores ($H_{in} < 7$ Å) compared to the Ar87PSD result. The chemical composition of the BPL sample is given in Table
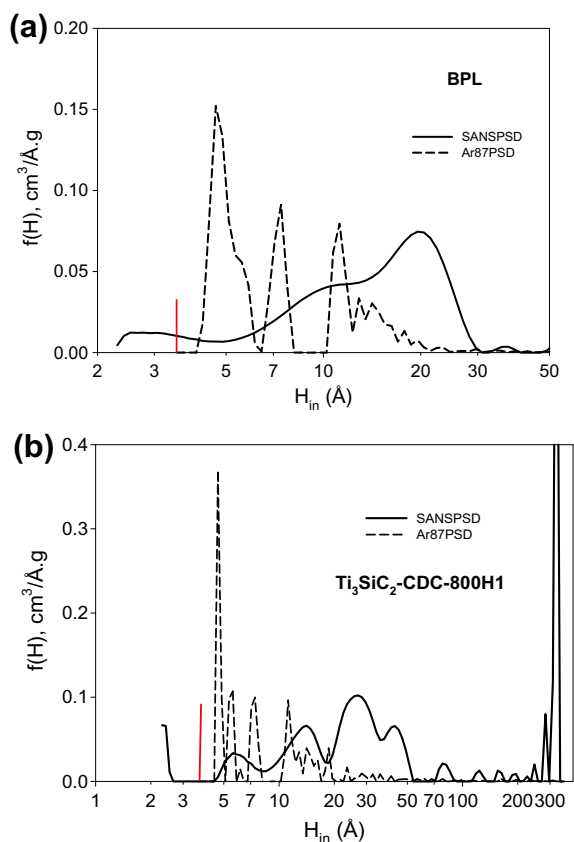
S1, and shows that the hydrogen content of BPL carbon is only a half of that of ACF-15 and Takeda 3 Å, but its contents of noncarbon atoms (O and S) are significantly larger than those of the latter samples. Furthermore, the ash content (3.11%) in BPL sample is much higher than that of Takeda 3 Å (0.61%). Consequently, among the three commercial carbon samples examined (Takeda 3 Å, ACF-15, and BPL) the impact of the scattering by the noncarbon atoms on the coherent scattering intensity in the high q region ($q > 0.6$ Å^{-1}) is expected to be least for the ACF-15. This is consistent with the best agreement between the SANSPSD and Ar87PSD results in the small pore population ($H_{in} < 7$ Å) found for the ACF-15 sample.

3.2.3. Ti$_3$SiC$_2$-CDC-800H1
Fig. 4b depicts the comparison between the SANSPSD and Ar87PSD results of the Ti$_3$SiC$_2$-CDC-800H1sample. From this figure, it can be seen that the SANSPSD result has an abnormally high population of mesopores ($H_{in} > 50$ Å), which could arise from interparticle spaces. Such large population of mesopores is similar to that in the distributions of carbonizate and its gasified forms with various burn-off degrees, determined from small angle scattering (SAXS) data by Gun'ko et al. [11]. It is interesting to see that despite the possible influence of the large population of mesopores (>50 Å) on the assumption of the infinitely dilute solution of polydisperse hollow spherical particles made in Eq. (6), there is a good agreement between the SANSPSD and Ar87PSD results in the small pore region (3.4 Å < H_{in} < 20 Å). Similar to the silicon carbon-derived carbons discussed in the Subsection 3.2.1, the SANSPSD result of the Ti$_3$SiC$_2$-CDC-800H1 sample also contains significant populations of ultramicropores ($H_{in} < 2.7$ Å) or mesopores (20 Å < H_{in} < 50 Å), which are inaccessible to Ar at 87 K. While a large population of mesopores (>50 Å) is present in the SANSPSD result of the Ti$_3$SiC$_2$-CDC-800H1, and in the PSD results of carbonizate and its gasified forms at various burn-off degrees, determined from small angle scattering (SAXS) data by Gun'ko et al. [11], a significant population of small pores ($H_{in} < 7$ Å) present in the Ti$_3$SiC$_2$-CDC-800H1 sample was surprisingly absent in the carbonizate samples.

Fig. 4 – Comparison between the SANSPSD and Ar87PSD results: (a) BPL and (b) Ti$_3$SiC$_2$-CDC-800H1.
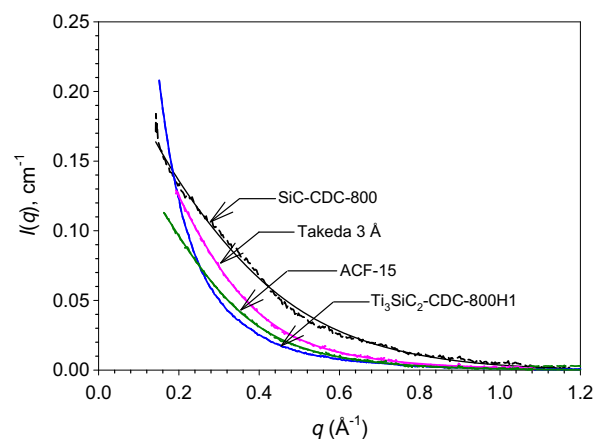
Fig. 5 – Comparison between the fitted SANS coherent intensity and the corresponding experimental curve for all the examined samples. Solid lines represent fitting results, and dashed lines the experimental curves.

Table 2 – Comparison of surface areas determined from the SANS and adsorption techniques.

Sample Name	2.3 Å < H_{in} < 3.4 Å		3.4 Å < H_{in} < 16.6 Å		42 Å > H_{in} > 16.6 Å		2.3 Å < H_{in} < 42 Å	
	S_u (SANS)	S_u (Ads)	S_{micro} (SANS)	S_{micro} (Ads)	S_{meso} (SANS)	S_{meso} (Ads)	S_t (SANS)	S_t (Ads)
SiC-CDC-800	505	0	1521	1821	184	19	2276	1846
Takeda 3 Å	30	0	385	660	37	7	431	668
BPL	85	0	789	1107	670	45	1612	1164
ACF-15	90	0	1151	1740	135	3	1419	1744

Note: the lower indices (u, micro, mes, and t) denotes ultra-micropores, micropores, mesopores, and total. Unit of the surface areas is given as m²/g.

Table 3 – Comparison of pore volumes determined from the SANS and adsorption techniques.

Sample Name	2.3 Å < H_{in} < 3.4 Å		42 Å > H_{in} > 16.6 Å		2.3 Å < H_{in} < 42 Å	
	V_u (SANS)	V_u (Ads)	V_{mes} (SANS)	V_{mes} (Ads)	V_t (SANS)	V_t (Ads)
SiC-CDC-800	0.070	0.000	0.240	0.052	0.909	0.608
Takeda 3 Å	0.034	0.000	0.039	0.008	0.245	0.172
BPL	0.012	0.000	0.776	0.049	1.240	0.472
ACF-15	0.013	0.000	0.154	0.005	0.737	0.540

Note: the lower indices (u, mes, and t) denotes ultra-micropores, mesopores, and total. Unit of the pore volumes is given as cm³/g.

Finally, Fig. 5 shows excellent fits of the theoretical neutron scattering intensities to the corresponding experimental data for all the carbon samples examined over the Porod range ($0.13 \text{ Å}^{-1} < q < 1.25 \text{ Å}^{-1}$). While there is significant impact of the scattering by the noncarbon atoms present in the BPL and Takeda 3 Å samples on the accuracy of their SANSPSD results, there is reasonably good agreement of the SANSPSD results of the remaining carbon samples examined (three carbide derived carbons and ACF-15), presented above, with the PSD results determined from Ar or CO_2 adsorption, and show the inaccessible pore spaces not probed by adsorption.

For clarity, we compared the surface areas and pore volumes derived from the SANS and adsorption techniques, as presented in Tables 2 and 3, for the carbon samples whose pore size distribution was successfully determined by the SANS technique. The values of the surface areas determined by the SANS technique were calculated from the SANSPSD results based on the slit-pore model assumed for these investigated carbon samples. In particular, the surface area was given as

$$S = \int \frac{2}{H} f(H) dH \tag{9}$$

Table 2 shows very good agreement in the surface areas of micropores ($3.4 \text{ Å} < H_{in} < 16.6 \text{ Å}$) obtained from the SANS and adsorption techniques for the examined SiCDC-800, for the pore size range but larger deviations exist for the commercial carbon samples (Takeda 3 Å and ACF-15, BPL). Furthermore, the total surface area of all the examined carbon samples determined by the SANS technique over the pore range size ($H_{in} < 42 \text{ Å}$) is generally smaller than that of a perfect graphene sheet (about 2630m²/g), as seen in Tables 2 and 3. From Tables 2 and 3 it is interesting to note that the significant fraction of the surface areas (500 m²/g) or pore volume in the ultra-micropore ranges, determined by the SANS

technique, are inaccessible to Ar at 87 K for the silicon carbide derived carbon sample. However, the small to moderate fractions (<100 m²/g) of the surface area inaccessible to CO_2 at 273 K for the Takeda 3 Å and Ar at 87 K for the remaining carbon samples (ACF-15 and BPL) may be due to the impact of scattering by the noncarbon atoms in this carbon, as discussed above. In practice, only part of the inaccessible surface areas or pore volumes may be opened during the early stage of gasification process, as discussed above. However, at higher degrees of the carbon burn-off the significant pore enlargements as well as removal of defect sites, which enhance the density of carbon fragments, will be the predominant mechanisms. Accordingly, as the degree of activation is increased the surface area of the carbon will at some point begin to decrease compared to that of its precursor. The relatively small surface area of this ultramicropore region (<3.4 Å) compared to that of the larger pore regions accessible to Ar or CO_2, could be due to a large population of molecularly narrow pore entries, which significantly slows the adsorption kinetics of small molecule such as CO_2 in Takeda 3 Å [26]. This is due to the small volume of the pore entry compared to its pore body.

It can be seen from Table 3 that except for the Takeda 3 Å CMS, which has small difference in mesopore volumes determined by the SANS and adsorption techniques, the remaining carbon samples have significantly larger fractions of mesopore volumes ($0.15–1.6 \text{ cm}^3/g$) determined by the SANS technique compared to those ($0.01–0.135 \text{ cm}^3/g$) obtained by the adsorption technique. The former mesopore volumes may be inaccessible to the Ar adsorption at 87 K, but will be opened for the Ar adsorption during the thermal treatment, as discussed above. Strong support for this conclusion of opening up of inaccessible porosity by heat treatment is provided by a comparison of the total SANS pore volume of SiC-CDC-800 of 0.909 cm^3/g, with the adsorption-based values of

1.064 cm^3/g for this carbon obtained after 3 days heat treatment at 1100 °C in Ar atmosphere [22]. It is clear that the adsorption-based values increase significantly and approach the SANS-based pore volumes upon heat treatment, indicative of increase in accessibility. Thus, the adsorption pore volume of 0.608 cm^3/g for the as-synthesised sample given in Table 2, while essentially identical to the theoretically expected [22] value of 0.61 cm^3/g, does not represent the true pore volume of the carbon, and considerable inaccessible porosity exists in the samples that is integrated into the accessible pore space by heat treatment. This inaccessible porosity must predominantly comprise of pore surface defects and roughness which are removed on heat treatment, as the surface area shows a much more modest increase on heat treatment compared to the increase in pore volume [22].

4. Conclusions

We carried out the interpretation of the small angle neutron scattering data for the average size of carbon particles as well as pore size distributions of five activated carbon samples (SiC-CDC-800, Ti$_3$SiC$_2$-CDC-800H1, BPL, MSC Takeda 3 Å, and ACF-15). We find significantly larger sized carbon particles in the samples (SiC-CDC-800, MSC Takeda 3 Å) with predominance of micropores (size <20 Å), than those in the other samples (Ti$_3$SiC$_2$-CDC-800H1 and BPL) which have high mass fractal degree and significant population of mesopores sized up to 48 Å. We also successfully determined the pore size distribution of the former group of the carbon samples (SiC-CDC-800, MSC Takeda 3 Å, BPL, and ACF-15) from the SANS data with the assumption of an infinitely dilute solution of hollow spherical particles However, this assumption is inapplicable to the Ti$_3$SiC$_2$-CDC-800H1 sample which contains significant population of large mesopores with high mass fractal degrees. Among these samples, the best agreement between the SANSPSD and Ar87PSD results achieved for the silicon carbide derived carbon sample indicates the relevance of SANS method to characterize the pore structure of pure microporous carbons such as carbide derived carbons. On the other hand, the presence of noncarbon species in the examined carbon samples (MSC Takeda 3 Å, BPL and ACF-15) leads to significant impact on the accuracy of the SANSPSD results of these carbons. The results from SANS show significant pore populations that are inaccessible to Ar and not probed during adsorption characterization by this gas. This inaccessible porosity largely comprises of surface defects that are removed on heat treatment or activation, so that while the inaccessible pore volume is incorporated into the accessible pore volume on heat treatment the surface area does not correspondingly increase.

Acknowledgments

Appendix A. Supplementary data

Supplementary data associated with this article can be found, in the online version, at doi:10.1016/j.carbon.2012.02.091.

REFERENCES

[1] Yushin G, Nikitin A, Gogotssi Y. In: Gogotsi Y, editor. Nanomaterials handbook. Boca Raton: CRC/Taylor & Francis; 2006. p. 239–82.

[2] Franklin RE. Crystallite growth in graphitizing and non-graphitizing carbons. Proc R Soc Lond A 1951;209(1097):196–218.

[3] Harris PJF, Liu Z, Suenaga K. Imaging the atomic structure of activated carbon. J Phys: Condens Matter 2008;20(36):362201–5.

[4] Nguyen TX, Bhatia SK. Determination of pore accessibility in disordered nanoporous materials. J Phys Chem C 2007;111(5):2122–222.

[5] Rios RVRA, Silvestre-Albero J, Sepúlveda-Escribano A, Molina-Sabio M, Rodríguez-Reinoso F. Kinetic restriction in the characterization of narrow microporosity in carbon materials. J Phys Chem C 2007;111(10):3803–5.

[6] Bae JS, Bhatia SK. High-pressure adsorption of methane and carbon dioxide on coal. Energy Fuels 2006;20(6):2599–607.

[7] Nguyen TX, Bhatia SK. Kinetic restriction of simple gases in porous carbons: transition-state theory study. Langmuir 2008;24(1):146–54.

[8] Hoinkis E, Ziehl M. A small-angle neutron scattering study of activated carbon fibers. Carbon 2003;41(11):2047–56.

[9] Calo JM, Hall PJ. The application of small angle scattering techniques to porosity characterization in carbons. Carbon 2004;42(7):1299–304.

[10] Laudisio G, Dash RK, Singer JP, Yushin G, Gogotsi Y, Fischer JE. Carbide-derived carbons: a comparative study of porosity based on small-angle scattering and adsorption isotherm. Langmuir 2006;22(21):8945–50.

[11] Gun'ko VM, Meikle ST, Kozynchenko OP, Tennison SR, Ehrburger-Dolle F, Morfin I, et al. Comparative characterization of carbon adsorbents and polymer precursors by small-angle x-ray scattering and nitrogen adsorption methods. J Phys Chem C 2011;115(21):10727–35.

[12] Cohaut N, Thery A, Guet JM, Rouzaud JN, Kocon L. The porous network in carbon aerogels investigated by small angle neutron scattering. Carbon 2007;45(16):1185–92.

[13] Nguyen TX, Cohaut N, Bae JS, Bhatia SK. New method for atomistic modeling of the microstructure of activated carbons using hybrid reverse Monte Carlo Simulation. Langmuir 2008;24(15):7912–22.

[14] Nguyen TX, Bae JS, Bhatia SK. Characterization and adsorption modeling of silicon carbide-derived carbons. Langmuir 2009;25(4):2121–32.

[15] Bae JS, Nguyen TX, Bhatia SK. Influence of synthesis conditions and heat treatment on the structure of Ti$_3$SiC$_2$-derived carbons. J Phys Chem C 2010;114(2):1046–56.

[16] Nguyen TX, Bhatia SK. Probing the pore wall structure of nanoporous carbons using adsorption. Langmuir 2004;20(9):3532–5.

[17] Nguyen TX, Bae JS, Wang Y, Bhatia SK. On the strength of the hydrogen-carbon interaction as deduced from physisorption. Langmuir 2009;25(8):4314–9.

[18] Glatter O, Kratky O. Small-angle X-ray scattering. London: Academic Press; 1982. p. 181–3.

[19] Welz S, McNallan MJ, Gogotsi Y. Carbon structures in silicon carbide derived carbon. J Mater Process Technol 2006;179(1–3):11–22.

[20] Hansen PC. The discrete Picard condition for discrete ill-posed problems. BIT 1990;30(4):658–72.

[21] Feng B, Bhatia SK. Variation of the pore structure of coal chars during gasification. Carbon 2003;41(3):507–23.

[22] Bonilla MR, Bae JS, Nguyen TX, Bhatia SK. Heat treatment-induced structural changes in SiC-derived carbons and their impacts on gas storage potential. J Phys Chem C 2010;114(39):16562–75.

[23] Glinka CJ. Incoherent neutron scattering from multi-element materials. J Appl Crystallogr 2011;44(3):618–24.

[24] Nguyen TX, Jobic H, Bhatia SK. Microscopic observation of kinetic molecular sieving of hydrogen isotopes in a nanoporous material. Phys Rev Lett 2010;105(8):085901–85904.

[25] Nguyen TX, Bhatia SK. Characterization of activated carbon fibers using argon. Carbon 2005;43(4):775–85.

[26] Gogotsi Y, Nikitin A, Ye H, Zhou W, Fischer JE, Yi B, et al. Nanoporous carbide-derived carbon with tunable pore size. Nat Mater 2003;2:591–4.